Highlights

Estimation of Sideslip Angle and Cornering Stiffness of an Articulated Vehicle Using a Constrained Lateral Dynamics Model

Dasol Jeong,Geonhee Ko,Seibum B. Choi

- Proposal of constrained lateral dynamics model of articulated vehicles.
- Model state reduction through physical constraints.
- Estimation of sideslip angle and cornering stiffness using a dual LTV Kalman filter.
- Experimental verification of estimation algorithm performance using an articulated bus.

Estimation of Sideslip Angle and Cornering Stiffness of an Articulated Vehicle Using a Constrained Lateral Dynamics Model

Dasol Jeong[a], Geonhee Ko[a] and Seibum B. Choi[a,*]

[a]Department of Mechanical Engineering, KAIST, 291 Daehak-ro Yuseong-gu, Daejeon, 34141, Republic of Korea

ARTICLE INFO

Keywords:
Articulated Bus
Articulated Vehicle
Constrained Lateral Dynamics Model
Cornering Stiffness
Dual Linear Time-varying Kalman Filter
Sideslip Angle

ABSTRACT

In this paper, a constrained lateral dynamics model of articulated vehicles and an algorithm for estimation of sideslip angle and cornering stiffness are proposed. The articulated vehicle was modeled using the bicycle model, linear tire model, and modified Dug-off model. The normal force of each axle included in the model was estimated based on the longitudinal load transfer model. Physical constraints were applied to reduce model states. Accurate sideslip angle and cornering stiffness are essential for vehicle control safety and autonomous driving performance. The sideslip angle and cornering stiffness were simultaneously estimated using a dual linear time-varying (LTV) Kalman filter. The observability matrix guaranteed the convergence of the proposed estimation algorithm. The estimation performance was verified by simulation with TruckSim and an experiment using an articulated bus.

1. Introduction

Currently, articulated vehicles are widely used as heavy trucks and commercial vehicles and have become the most important vehicles in freight transport. In public transportation systems, articulated buses have been developed and used, including such as Phileas in The Netherlands, bimodal trams in Korea, and Lancaster in the USA [1], [2]. Heavy-duty trucks (including articulated vehicles) have a large load capacity and provide efficient transport, but have the disadvantage of economic and human damage in case of an accident [3]. There is also a disadvantage in terms of vehicle stability due to the characteristics of articulated vehicles: heavy mass and high center of mass [4]. Therefore, the modeling, control, and state estimation of articulated vehicles constitute important research in the field of vehicle systems and control.

A number of improvements have been proposed in previous studies of articulated vehicles, including roll dynamics to prevent roll-over [5], active chaos control through pitch dynamics modeling [6], a lateral model for all-wheel steering vehicles [7], and a model for differential braking control [8]. In most previous studies, many states were used due to the characteristics of articulated vehicles. In [9], a seven degrees-of-freedom (DOF) model was proposed to estimate the hitch force and tire lateral force. To guarantee observability, longitudinal tire force and lateral velocity (which are difficult to know in practice) were used. Models using many states cannot guarantee observability with typical measurements. Moreover, complex modeling and algorithms have disadvantages in calibration issues, time-consuming, and real-time applications. Model state reduction can be used as a solution to the above problems. In this paper, the number of states was reduced using physical constraints.

*Corresponding author
oieiaa@kaist.ac.kr (D. Jeong); ghmichael@kaist.ac.kr (G. Ko); sbchoi@kaist.ac (S.B. Choi)
ORCID(s):

The sideslip angle is an essential vehicle state that must be known for vehicle safety and effective autonomous driving systems [10]. Because the sideslip angle cannot be measured directly, estimation algorithms have been proposed for that purpose. In previous studies, sideslip angle estimation algorithms were classified as either kinematics-based or dynamics-based algorithms [11]. Kinematics-based algorithms estimate the sideslip angle based on vehicle velocity and acceleration. This method has the advantage that it is not affected by tire-road friction parameters and dynamic properties [12]. It uses a strategy to estimate the sideslip angle in the form of an integrator. The integral estimation strategy has the disadvantage in that a cumulative estimation error occurs. Recently, sideslip angle estimation algorithms using a global positioning system (GPS) signal have been studied. In combination with GPS, sideslip angle estimation algorithms using an event trigger [13], a neural network [14], and a magnetometer with GPS [15] have been proposed. However, GPS signals have the disadvantages of being noisy and having a low sampling rate. Moreover, the GPS reception rate and accuracy decreases in urban areas, and the cumulative estimation error increases because the estimation algorithm works with a simple integrator [16].

Dynamics-based sideslip estimation algorithms consider vehicle dynamics and tire forces. The full-car model and bicycle model were used as vehicle dynamics models. The full-car model has the advantage of accurately depicting vehicle dynamics because it models the forces of all the tires. However, many parameters were introduced and used and most previous studies assumed that the values of these parameters were known [17]. In contrast, the bicycle model describes the lateral dynamics of the vehicle as a 2 DOF model. Because of this, fewer states and parameters are used. Because of these advantages, the bicycle model has been widely used [11]. The tire models used included nonlinear tire models with combined longitudinal and lateral slip, along with linear tire models with a pure lateral slip angle. In [18], tires were modeled using the brush tire model and the

sideslip angle was estimated using an interacting multiple model Kalman filter. In [19], the longitudinal and lateral velocities were estimated by modeling the tire force using the LuGre model. However, both algorithms assumed that the parameters representing the tire characteristics were known. The exact value of these tire parameters was unknown, and inaccurate values caused poor estimation performance [20]. In contrast, the linear tire model expressed the lateral force and the tire sideslip angle in a linear relationship. Moreover, only one tire parameter, cornering stiffness, was used. Therefore, the feasibility of estimating unknown parameters was high. However, the linear tire model does not describe the force well when the longitudinal slip ratio and lateral slip angle are combined. Nevertheless, the linear tire model has often been used because of its simplicity and good performance for pure lateral slip [11].

A range of models, from complex to simple, have been studied to represent vehicle dynamics and tire forces. Using complex models requires many parameters. These values have a significant impact on estimation performance [20] and sometimes on change [21]. Therefore, it is necessary to design a parameter estimator to ensure the estimation performance and validity of a complex model when it is used. However, typical automotive sensors alone cannot guarantee observability when estimating many parameters and states. In [22], algorithms for estimating brush tire model parameters and tire forces were proposed. However, to ensure observability, it was assumed that the sideslip angle and slip ratio were known. A limitation of using complex models is that unknown parameters (or states) are often used. Therefore, in this study, we tried to describe the lateral dynamics of an articulated vehicle using a simple model, to avoid the use of unknown parameters or states. Vehicle dynamics and tire forces were modeled using the bicycle model and the linear tire model. In other words, in this study, lateral dynamics modeling for articulated vehicles was performed by focusing on the pure slip angle situation and the linear sideslip region.

Cornering stiffness is the ratio of the tire slip angle and lateral force. Inaccurate cornering stiffness adversely affects sideslip angle estimation performance. Therefore, the sideslip angle and cornering stiffness should be estimated simultaneously. For general passenger cars, a beta-less estimation algorithm [23], estimation using an extended Kalman filter [24], and estimation using GPS [25] have been proposed. For articulated vehicles, a cornering stiffness estimation algorithm using a dual Kalman filter [26] has been proposed. Most studies have used the first order Dug-off model and assumed that the nominal cornering stiffness was known. However, cornering stiffness cannot be said to be perfectly linear with a normal load, and nominal cornering stiffness changes with the road surface and tires. For accurate estimation, it is essential to estimate the absolute cornering stiffness value using the modified tire model.

Algorithms for estimating states and parameters at the same time are classified into two types according to the method used for parameter adaptation. There are Lyapunov function-based methods (such as adaptive observers [27], [28]) and Kalman filter-based methods (such as extended Kalman filters [29], interactive multi-modal algorithms [30], and dual Kalman filters [31], [32]). Adaptive observers have advantages in terms of computational time [27]. Moreover, intuitive design of an observer is possible through the Lyapunov function [28]. However, it shows weakness because '*a posteriori*' information is not used in parameter estimation. Conversely, in the case of the Kalman filter-based method, robust observer design is possible because parameters are estimated using '*a posteriori*' information. Among these Kalman filter-based algorithms, the extended Kalman filter, which uses augmented states, and the interactive multi-model algorithm, which uses multiple models and Kalman filters, required long computation times. On the other hand, the dual Kalman filter, which estimated states and parameters using two Kalman filters, requires a relatively short calculation time [31].

Figure 1: Articulated bus and experimental set-up

In this paper, we propose a constrained lateral dynamics model and an algorithm for estimating sideslip angle and cornering stiffness. Articulated vehicles with complex dynamics and many states were used for modeling. Physical constraints were used to reduce the number of states modeled. The proposed model can describe dynamics in fewer states than the previous models and has advantages in calibration issues, calculation time, and observability. The sideslip angle and cornering stiffness were estimated using the dual linear time-varying (LTV) Kalman filter. Vehicle states, including the sideslip angle, were estimated in the first Kalman filter. The cornering stiffness was estimated in the second Kalman filter using the output residual and '*a posteriori*' information. The estimation stability is guaranteed by using an observability matrix [33]. The proposed estimation algorithm was verified through simulation using TruckSim and by an experiment performed using an articulated bus equipped with two RT3000s as shown in Fig. 1.

The rest of the paper is organized as follows. In Section 2, constrained lateral dynamics model for articulated vehicles is proposed with physical constraints. In Section 3, the cornering stiffness and sideslip angle estimation algorithm using the dual LTV Kalman filter is proposed. The simulation and experimental results are provided in Sections 4 and 5. Conclusions are provided in Section 6.

Table 1
Specifications of the articulated bus used in the experiment.

Symbol	Parameter	Value
m_1	Total mass of front unit	$11180\,kg$
m_2	Total mass of rear unit	$10130\,kg$
m_{1u}	Unsprung mass of 1^{st} axle	$350\,kg$
m_{2u}	Unsprung mass of 2^{nd} axle	$350\,kg$
m_{3u}	Unsprung mass of 3^{rd} axle	$350\,kg$
I_1	Yaw inertia of front unit	$60193\,kgm^2$
I_2	Yaw inertia of rear unit	$54540\,kgm^2$
l_{f1}	Distance between 1^{st} axle to CG_1	$4.6260\,m$
l_{r1}	Distance between 2^{nd} axle to CG_1	$3.0840\,m$
P_1	Distance between 2^{nd} axle to hitch	$1.123\,m$
l_{f2}	Distance between hitch to CG_2	$3.8712\,m$
l_{r2}	Distance between 3^{rd} axle to CG_2	$2.5808\,m$
C_1	Cornering stiffness of the 1^{st} axle	$\sim 4E05\,N/rad$
C_2	Cornering stiffness of the 2^{nd} axle	$\sim 7E05\,N/rad$
C_3	Cornering stiffness of the 3^{rd} axle	$\sim 5E05\,N/rad$

Table 2
States of the articulated vehicle.

Symbol	Parameter	Unit
δ	Front wheel steering angle	rad
β_i	Sideslip angle of the i^{th} unit	rad
r_i	Yaw rate of the i^{th}unit	rad/s
α	Articulated angle	rad
σ_{xi}	Tire slip ratio of the i^{th} axle	$-$
σ_{yi}	Tire sidealip angle of the i^{th} axle	rad
v_{xi}	Longitudinal velocity of the i^{th} unit	m/s
v_{yi}	Lateral velocity of the i^{th} unit	m/s
a_{xi}	Longitudinal acceleration of the i^{th} unit	m/s^2
a_{yi}	Lateral acceleration of the i^{th} unit	m/s^2
F_{xi}	Longitudinal force of the i^{th} axle	N
F_{yi}	Lateral force of the i^{th} axle	N
F_{zi}	Normal force of the i^{th} axle	N
F_{xh}	Longitudinal force of hitch	N
F_{yh}	Lateral force of hitch	N
Δt	Sampling time	s

2. CONSTRAINED LATERAL DYNAMICS MODEL FOR ARTICULATED VEHICLES

The constrained lateral dynamics model for articulated vehicles was proposed in order to estimate the sideslip angle and cornering stiffness. The bicycle and linear tire models were used to ensure observability. These models showed good performance for estimating the pure sideslip angle and linear sideslip angle regions. Therefore, the following assumptions were applied to the modeling:

- The tire sideslip angle is in the linear sideslip angle-lateral force region.

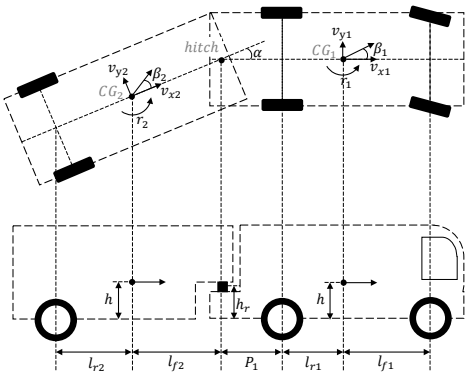

Figure 2: The coordinate system of articulated vehicles

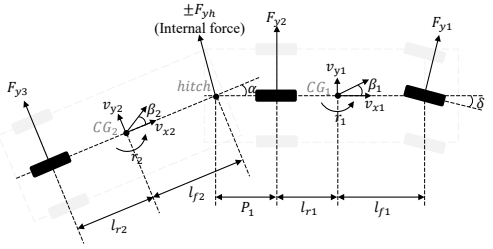

Figure 3: The bicycle model of articulated vehicles

$$
\begin{aligned}
&|\sigma_{y1}|, |\sigma_{y2}|, |\sigma_{y3}| << 1 \\
&\text{where } \sigma_{y1} = \beta_1 + \frac{l_{f1}}{v_{x1}} r_1 - \delta, \\
&\sigma_{y2} = \beta_1 - \frac{l_{r1}}{v_{x1}} r_1, \sigma_{y3} = \beta_2 - \frac{l_{r2}}{v_{x2}} r_2
\end{aligned}
\tag{1}
$$

- The tire slip ratio is negligible.

$$
\begin{aligned}
&\sigma_{x1}, \sigma_{x2}, \sigma_{x3} \approx 0 \\
&\text{where } \sigma_{x1} = \frac{R_{eff,1}\omega_1 - v_{x1}}{v_{x1}}, \\
&\sigma_{x2} = \frac{R_{eff,2}\omega_2 - v_{x1}}{v_{x1}}, \sigma_{x3} = \frac{R_{eff,3}\omega_3 - v_{x2}}{v_{x2}},
\end{aligned}
\tag{2}
$$

The cornering stiffness was modeled using the modified Dug-off model. Moreover, a longitudinal load transfer model and physical constraints were proposed. Finally, a constrained lateral dynamics model was proposed for articulated vehicles. The coordinate system of an articulated bus is shown in Fig. 2. The specifications and states of the articulated vehicle used in the experiments are shown in Tables 1 and 2, respectively.

2.1. Bicycle model of articulated vehicles

The bicycle model describes the vehicle as a 2 DOF model. The bicycle model has the advantage of being able to describe complex vehicle models simply [34]. The articulated vehicle bicycle model used in this paper is shown in Fig. 3. From previous assumptions, the longitudinal force was assumed to be zero, and the steering angle and articulated angle were assumed to be very small. The force/torque

balance equation based on the center of gravity (CG point) of the front unit and rear unit is as follows:

$$\begin{aligned} m_1 a_{y1} &= F_{yh}\cos\alpha + F_{y1}\cos\delta + F_{y2} \\ &\approx F_{yh} + F_{y1} + F_{y2} \\ m_2 a_{y2} &= -F_{yh} + F_{y3} \end{aligned} \tag{3}$$

$$\begin{aligned} I_1\dot{r}_1 &= -(P_1 + l_{r1})F_{yh}\cos\alpha + l_{f1}F_{y1}\cos\delta - l_{r1}F_{y2} \\ &\approx -(P_1 + l_{r1})F_{yh} + l_{f1}F_{y1} - l_{r1}F_{y2} \\ I_2\dot{r}_2 &= -l_{f2}F_{yh} - l_{r2}F_{y3} \end{aligned} \tag{4}$$

The kinematic constraints for the lateral acceleration and articulated angle were used as shown in the equation below.

$$\begin{aligned} a_{y1} &= r_1 v_{x1} + \dot{\beta}_1 v_{x1} \\ a_{y2} &= r_2 v_{x2} + \dot{\beta}_2 v_{x2} \\ \dot{\alpha} &= r_2 - r_1 \end{aligned} \tag{5}$$

The bicycle model of articulated vehicles was used in combination with the tire model and physical constraints.

2.2. Tire model

A vehicle's pneumatic tires generate longitudinal and lateral forces that play a key role in vehicle motions. Because tires are made of complex materials, modeling tire force is a huge challenge. In previous studies, tire models such as the Pacejka model [35], the Brush tire model [22], and the flexible ring tire model [36] have been studied. However, these nonlinear tire models were difficult to apply to vehicle dynamics because they used many tire model parameters. Among the nonlinear tire models, the most frequently used brushed tire models are:

$$F_{xi} = \frac{C_{xi}\left(\frac{\sigma_{xi}}{1+\sigma_{xi}}\right)}{f_i}F_i,\ F_{yi} = -\frac{C_i\left(\frac{\tan\sigma_{yi}}{1+\sigma_{xi}}\right)}{f_i}F_i,$$

where

$$F_i = \begin{cases} f_i - \dfrac{1}{3\mu F_{zi}}f_i^2 + \dfrac{1}{27\mu^2 F_{zi}^2}f_i^3, & \text{if } f_i \le 3\mu F_{zi} \\ \mu F_{zi}, & \text{else} \end{cases} \tag{6}$$

$$f_i = \sqrt{C_{xi}^2\left(\frac{\sigma_{xi}}{1+\sigma_{xi}}\right)^2 + C_i^2\left(\frac{\tan\sigma_{yi}}{1+\sigma_{xi}}\right)^2}$$

where C_{xi} is the longitudinal stiffness of the i^{th} axle, C_i is the cornering stiffness of the i^{th} axle, and μ is the tire-road friction coefficient.

In this study, tire forces were modeled using the linear tire model. The linear tire model is the relationship between the lateral tire force and the sideslip angle at a small slip ratio and sideslip angle. The tire force by the linear tire model is defined in (7). The linear tire model is suitable for describing tire force when the tire slip angle is small.

$$F_{yi} \approx \left.\frac{\partial F_{yi}}{\partial\sigma_{yi}}\right|_{\sigma_{xi}=\sigma_{yi}=0}\sigma_{yi} = -C_i\sigma_{yi} \tag{7}$$

Moreover, the tire slip angle and tire lateral force have a linear relationship, which does not harm the linearity of the vehicle model. Eq. (8) shows the lateral tire force on each axle expressed through the linear tire model.

$$\begin{aligned} F_{y1} &= -C_1\alpha_1 = -C_1\left(\beta_1 + \frac{l_{f1}}{v_{x1}}r_1 - \delta\right) \\ F_{y2} &= -C_2\alpha_2 = -C_2\left(\beta_1 - \frac{l_{r1}}{v_{x1}}r_1\right) \\ F_{y3} &= -C_3\alpha_3 = -C_3\left(\beta_2 - \frac{l_{r2}}{v_{x2}}r_2\right) \end{aligned} \tag{8}$$

In (8), the cornering stiffness of each axle was used. In previous studies, the Dug-off model was used, which assumed that the cornering stiffness had a linear relationship with the normal force. However, the cornering stiffness is not perfectly linear with the normal force. According to [17], the cornering stiffness is expressed as a second-order polynomial of the normal force. This tire model was called a modified Dug-off model in previous studies. The cornering stiffness of each axle is expressed by (9).

$$C_i = aF_{zi} - bF_{zi}^2 \tag{9}$$

where a and b are cornering stiffness parameters and F_{zi} is the i^{th} axle normal force. Through the linear tire model and modified Dug-off model, the lateral force of each axle is expressed as (10).

$$\begin{aligned} F_{y1} &= -\left(aF_{z1} - bF_{z1}^2\right)\times\left(\beta_1 + \frac{l_{f1}}{v_{x1}}r_1 - \delta\right) \\ F_{y2} &= -\left(aF_{z2} - bF_{z2}^2\right)\times\left(\beta_1 - \frac{l_{r1}}{v_{x1}}r_1\right) \\ F_{y3} &= -\left(aF_{z3} - bF_{z3}^2\right)\times\left(\beta_2 - \frac{l_{r2}}{v_{x2}}r_2\right) \end{aligned} \tag{10}$$

Here, (10) expresses three cornering stiffness (C_1, C_2, C_3) as two cornering stiffness parameters (a, b). This shows the result of reducing the number of unknown parameters from three to two. The reduction in the number of unknown parameters plays an important role in the observability analysis in Section 3.2.

2.3. Algorithm for estimating the normal force of each axle

In (10) the normal force of each axle was used. The normal force on each axle was estimated through vehicle specifications and the longitudinal load transfer model. The longitudinal load transfer model of the articulated vehicle used is shown in Fig. 4. The load transfer was modeled based on the sprung mass and unsprung mass. Total mass is defined as the sum of the sprung mass and unsprung mass as in (11). Moreover, because the unsprung mass was very small compared to the sprung mass, it was assumed that the

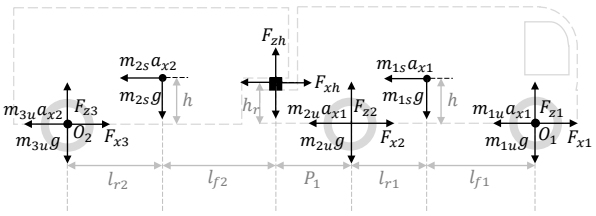

Figure 4: Longitudinal load transfer model for an articulated vehicle

CG point of the sprung mass is the same as the CG point of gravity of total mass.

$$\begin{aligned} m_1 &= m_{1s} + m_{1u} + m_{2u} \\ m_2 &= m_{2s} + m_{3u} \end{aligned} \tag{11}$$

For the front unit and rear unit, the force balance equations in the X and Z directions are expressed as in (12) and (13), and the torque balance equations at O1 and O2 are expressed as (14). In the torque balance equation, it was assumed that the pitch acceleration is zero.

- Force balance equation in longitudinal direction

$$\begin{aligned} m_1 a_{x1} + m_2 a_{x2} &= F_{x1} + F_{x2} + F_{x3} \\ m_1 a_{x1} &= F_{x1} + F_{x2} + F_{xh} \end{aligned} \tag{12}$$

- Force balance equation in vertical direction

$$\begin{aligned} m_1 g + m_2 g &= F_{z1} + F_{z2} + F_{z3} \\ m_1 g &= F_{z1} + F_{z2} + F_{zh} \end{aligned} \tag{13}$$

- Torque balance equation in O_1 and O_2

$$\begin{aligned} (l_{f1} + l_{r1})F_{z2} - h m_{1s} a_{x1} - l_{f1} m_{1s} g - (l_{f1} + l_{r1}) m_{2u} g \\ + h_r F_{xh} + (l_{f1} + l_{r1} + P_1) F_{zh} = 0 \\ -h m_{2s} a_{x2} + l_{r2} m_{2s} g - h_r F_{xh} + (l_{f2} + l_{r2}) F_{zh} = 0 \end{aligned} \tag{14}$$

Articulated vehicles have different load transfers depending on the longitudinal force of each axle due to the hitch characteristics. In this study, an articulated vehicle with front-wheel drive was used. Therefore, when accelerating ($a_{x1} > 0$ and $a_{x2} > 0$), the first axle was used as the driveshaft. During deceleration ($a_{x1} < 0$ and $a_{x2} < 0$), it was assumed that the braking force of each axle was proportional to the brake pressure as follow:

$$\epsilon_3 = \frac{F_{x3}}{F_{x1} + F_{x2} + F_{x3}} = \frac{Br_3}{Br_1 + Br_2 + Br_3} \tag{15}$$

where Br_i is the brake pressure of the i_{th} axle. Through the force and torque balance equations and (15), the normal force of each axle during acceleration and deceleration is expressed as in (16) and (17).

- Normal force of each axle during acceleration

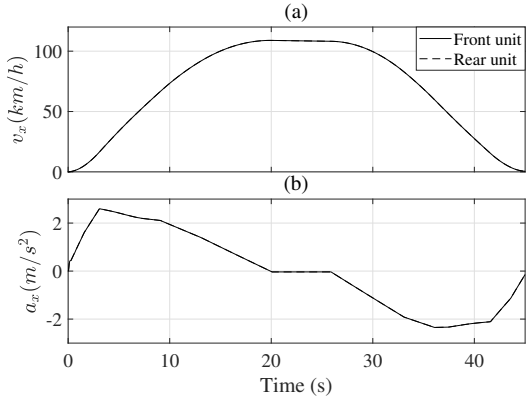

Figure 5: Simulation scenario: (a) Longitudinal velocity of front unit and rear unit (b) Longitudinal acceleration of front unit and rear unit

$$\begin{aligned} \mathbf{F} &= \mathbf{LS} \times g + \mathbf{LT_1} \times a_{x1} + \mathbf{LT_2} \times a_{x2}, \\ \text{where} \quad \mathbf{F} &= \begin{bmatrix} F_{z1} \\ F_{z2} \\ F_{z3} \end{bmatrix}, \quad \mathbf{LT_1} = \begin{bmatrix} -\frac{h}{L_1} \\ \frac{h}{L_1} \\ 0 \end{bmatrix} m_{1s}, \\ \mathbf{LT_2} &= \begin{bmatrix} \frac{P_1 h}{L_1 L_2} \\ -\frac{h(L_1+P_1)}{L_1 L_2} \\ \frac{h}{L_2} \end{bmatrix} m_{2s} + \begin{bmatrix} -\frac{h_r(P_1+L_2)}{L_1 L_2} \\ \frac{h_r(L_1+P_1+L_2)}{L_1 L_2} \\ -\frac{h_r}{L_2} \end{bmatrix} m_2, \\ \mathbf{LS} &= \begin{bmatrix} \frac{l_{r1}}{L_1} \\ \frac{l_{f1}}{L_1} \\ 0 \end{bmatrix} m_{1s} + \begin{bmatrix} \frac{-P_1 l_{r2}}{L_1 L_2} \\ \frac{(L_1+P_1) l_{r2}}{L_1 L_2} \\ \frac{l_{f2}}{L_2} \end{bmatrix} m_{2s} + \begin{bmatrix} m_{1u} \\ m_{2u} \\ m_{3u} \end{bmatrix}, \\ L_1 &= l_{f1} + l_{r1}, \quad L_2 = l_{f2} + l_{r2} \end{aligned} \tag{16}$$

- Normal force of each axle during braking

$$\begin{aligned} \mathbf{F} &= \mathbf{LS} \times g + \mathbf{LT_1} \times a_{x1} + \mathbf{LT_2} \times a_{x2} + \mathbf{Br}, \\ \text{where } \mathbf{Br} &= \begin{bmatrix} \frac{h_r(P_1+L_2)}{L_1 L_2} \\ -\frac{h_r(L_1+P_1+L_2)}{L_1 L_2} \\ \frac{h_r}{L_2} \end{bmatrix} \left(m_1 a_{x1} + m_2 a_{x2} \right) \epsilon_3 \end{aligned} \tag{17}$$

As shown in (16) and (17), the normal force of each axle for acceleration and deceleration was estimated using the vehicle specifications and acceleration signals. Because there was no equipment capable of measuring the normal force during the experiment, the estimation performance was verified by simulation using TruckSim. The vehicle plant used in TruckSim had the same specification as the articulated bus used in the experiment. The simulation scenarios selected are shown in Fig. 5. The normal force of each axle estimation result is shown in Fig. 6. The estimation algorithm had a root mean square (RMS) error of 1 %. This means that the estimated values are accurate enough to be used in the model. The estimation performance can be improved if the effect of pitch dynamics is considered.

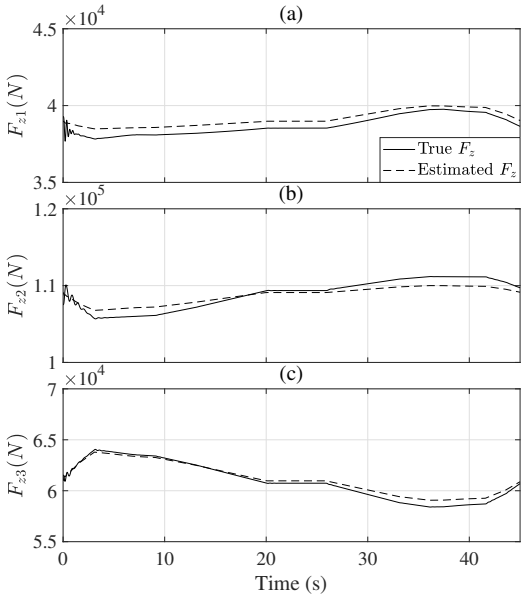

Figure 6: Simulation results from estimating the normal force: (a) First axle normal force (b) Second axle normal force (c) Third axle normal force

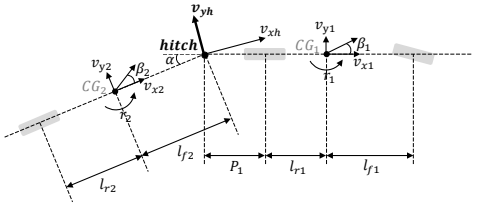

Figure 7: Physical constraint 1: Lateral velocity at the hitch point

2.4. Physical constraints

In this section, the reduction of the number of model states using physical constraints is introduced. The physical constraints were analyzed in terms of lateral velocity and lateral force at the hitch point. We assumed the articulated angle and the steering angle are small ($|\alpha| \ll 1, |\delta| \ll 1$) and that the longitudinal velocities of the front and rear units are the same ($v_{x1} = v_{x2} = v_x$). Physical constraints were used to allow the creation of the proposed constrained articulated lateral dynamics model.

- Lateral velocity at the hitch point

Articulated vehicles have geometric movements, as shown in Fig. 7. The hitch point is the kinematic connection between the front unit and the rear unit. Therefore, the lateral velocities at the hitch point calculated for the front unit and rear unit have to be equal. In (18), the middle side and right side represent the lateral velocity calculated through the front unit and rear unit.

$$v_{yh} = v_{y1} - (l_{r1} + P_1)r_1 = v_x\alpha + (v_{y2} + l_{f2}r_2) \quad (18)$$

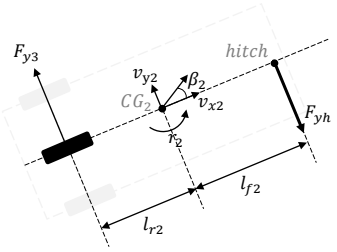

Figure 8: Physical constraint 2: Lateral force at the hitch point

Eq. (18) can be expressed as (19)

$$\beta_2 = \beta_1 - \alpha - \frac{(l_{r1} + P_1)r_1 + l_{f2}r_2}{v_x} \quad (19)$$

Here, (19) expresses the sideslip angle of the rear unit in terms of the sideslip angle of the front unit and its measurement. Through (19), it was verified that the sideslip angle of the front unit and of the rear unit was dependent. Through the lateral velocity of the hitch point constraint, the sideslip angle of the rear unit (β_2) can be expressed using the remaining states. This means that reduction of the number of states modeled was achieved.

- Lateral force at the hitch point

A second physical constraint was proposed to act through the lateral force at the hitch point. The lateral states and forces of the rear unit are shown in Fig. 8. At the center of gravity (CG) point of the rear unit, the force/torque balance equation is:

$$\begin{aligned} m_2 a_{y2} &= -F_{yh} + F_{y3} \\ I_2 \dot{r}_2 &= -l_{f2}F_{yh} - l_{r2}F_{y3} \end{aligned} \quad (20)$$

Through (20), the lateral force at the hitch point can be expressed as (21).

$$F_{yh} = -\frac{l_{r2}m_2 a_{y2} + I_2\dot{r}_2}{l_{f2} + l_{r2}} \quad (21)$$

Substituting (5) and (19) into (21), the lateral force at the hitch point can be expressed as (22).

$$\begin{aligned} F_{yh} = &-\frac{l_{r2}}{l_{f2} + l_{r2}} m_2 v_x \\ &\times \left(\dot{\beta}_1 + r_1 - \frac{l_{r1} + P_1}{v_x}\dot{r}_1 + \frac{I_2 - l_{f2}l_{r2}m_2}{l_{r2}m_2 v_x}\dot{r}_2 \right) \end{aligned} \quad (22)$$

Here, (22) expresses the lateral force at the hitch force as a combination of vehicle states. The lateral force at the hitch point cannot be measured by vehicle sensors, but it plays an important role in the lateral dynamics. Analysis of the lateral force at the hitch point was used to improve the modeling as well as to reduce the state number.

2.5. Constrained lateral dynamics model for articulated vehicles

In this section, the constrained articulated lateral dynamics model is proposed that uses the bicycle model, tire model, normal force estimation, and physical constraints. In the proposed model, four vehicle states (v_{y1}, r_1, r_2, α), one input (δ), and three outputs (r_1, r_2, α) were used. The final form of the proposed model was created by substituting (5),(10),(19), and (22) into the bicycle model shown in (3) and (4). The proposed constrained articulated lateral dynamics model is shown in (23).

$$
\begin{gathered}
\text{Let, } \mathbf{x} = \begin{bmatrix} v_{y1} & r_1 & r_2 & \alpha \end{bmatrix}^T, \mathbf{u} = \delta, \mathbf{y} = \begin{bmatrix} r_1 & r_2 & \alpha \end{bmatrix}^T \\
\dot{\mathbf{x}} = \mathbf{A}\mathbf{x} + \mathbf{B}\mathbf{u}, \mathbf{y} = \mathbf{C}\mathbf{x}, \\
\text{where } \mathbf{A} = \mathbf{T_0^{-1}}\mathbf{A_0}, \mathbf{B} = \mathbf{T_0^{-1}}\mathbf{B_0},
\end{gathered}
$$

$$
\mathbf{T_0} = \begin{bmatrix}
1 + \frac{l_{r2}}{L_2}\frac{m_2}{m_1} & -\frac{l_{r2}(P_1+l_{r2})}{L_2}\frac{m_2}{m_1} & \frac{1}{L_2}\frac{I_2 - l_{f2}l_{r2}m_2}{m_1} & 0 \\
-\frac{(P_1+l_{r1})l_{r2}}{L_2}\frac{m_2}{I_1} & 1 + \frac{(P_1+l_{r1})^2 l_{r2}}{L_2}\frac{m_2}{I_1} & -\frac{P_1+l_{r1}}{L_2}\frac{I_2 - l_{f2}l_{r2}m_2}{I_1} & 0 \\
-\frac{l_{f2}l_{r2}}{L_2}\frac{m_2}{I_1} & 1 + \frac{(P_1+l_{r1})^2}{L_2}\frac{m_2}{I_1} & \frac{l_{r2}}{L_2}\frac{I_2 + l_{f2}^2 m_2}{I_2} & 0 \\
0 & 0 & 0 & 1
\end{bmatrix},
$$

$$
\mathbf{A_0} = \begin{bmatrix}
-\frac{C_1+C_2}{m_1 v_x} & \frac{-C_1 l_{f1} + C_2 l_{r1}}{m_1 v_x} - \left(1 + \frac{l_{r2}}{L_2}\frac{m_2}{m_1}\right) v_x & 0 & 0 \\
\frac{-C_1 l_{f1} + C_2 l_{r1}}{I_1 v_x} & \frac{-C_1 l_{f1}^2 - C_2 l_{r1}^2}{I_1 v_x} + \frac{(P_1+l_{r1})l_{r2}}{L_2}\frac{m_2 v_x}{I_1} & 0 & 0 \\
\frac{C_3 l_{r2}}{I_2 v_x} & \frac{-C_1 l_{r2}(P_1+l_{r1})}{I_2 v_x} + \frac{l_{f2} l_{r2}}{L_2}\frac{m_2 v_x}{I_2} & -\frac{C_3 l_{r2} L_2}{I_2 v_x} - \frac{C_3 l_{r2}}{I_2} & 0 \\
0 & -1 & 1 & 0
\end{bmatrix},
$$

$$
\mathbf{B_0} = \begin{bmatrix} \frac{C_1}{m_1} \\ \frac{C_1 l_{f1}}{I_1} \\ 0 \\ 0 \end{bmatrix}, \mathbf{C} = \begin{bmatrix} 0 & 1 & 0 & 0 \\ 0 & 0 & 1 & 0 \\ 0 & 0 & 0 & 1 \end{bmatrix},
$$

$$
C_i = aF_{zi} - bF_{zi}^2 \tag{23}
$$

In Section 2, articulated vehicles were modeled using the bicycle model and the tire model. The modified Dug-off model was used to express three cornering stiffness as two cornering stiffness parameters. Reducing the number of parameters played an important role in the observability analysis in Section 3.2. The modified Dug-off model uses a normal force of each axle, each oh which was estimated using a longitudinal load transfer model. Physical constraints were introduced for state reduction and improved the modeling. Finally, the constrained articulated vehicle model was proposed. Compared with previous models, the proposed model can describe lateral dynamics with only four states. This has advantages in terms of computation time and estimation stability of the algorithm.

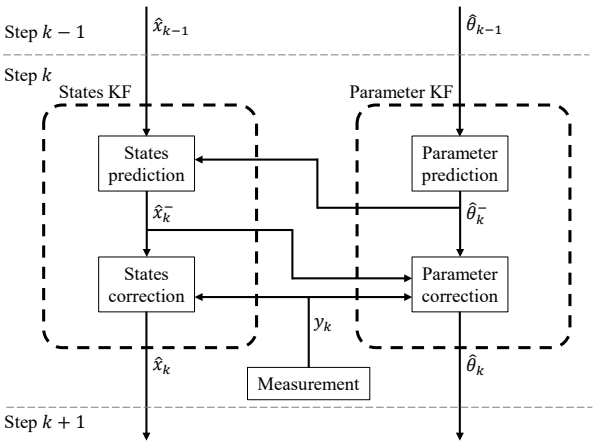

Figure 9: Schematic of the dual LTV Kalman filter

3. ALGORITHM FOR ESTIMATING SIDESLIP ANGLE AND CORNERING STIFFNESS

In Section 3, the algorithm for estimating the sideslip angle and cornering stiffness using the constrained articulated vehicle model is proposed. The dual LTV Kalman filter was used as the estimation method. As shown in Fig. 9, the estimation algorithm consists of two Kalman filters. The sideslip angle was estimated by the left Kalman filter and the cornering stiffness was estimated by the right Kalman filter.

3.1. Dual LTV Kalman filter for estimation of sideslip angle and cornering stiffness

The dual LTV Kalman filter was used to estimate the sideslip angle and cornering stiffness. The dual LTV Kalman filter consists of the state Kalman filter and the parameter Kalman filter [37]. Each Kalman filter contains prediction and correction stages. In this section, the proposed dual LTV Kalman filter is introduced.

- Discretization of system dynamics

Here, (23) is expressed in the form of (24) in the discrete-time domain.

$$
\begin{gathered}
\text{Let, } \mathbf{x}_k = \begin{bmatrix} v_{y1}(k) & r_1(k) & r_2(k) & \alpha(k) \end{bmatrix}^T, \mathbf{u}_k = \delta(k), \\
\mathbf{y}_k = \begin{bmatrix} r_1(k) & r_2(k) & \alpha(k) \end{bmatrix}^T, \theta_k = \begin{bmatrix} a(k) & b(k) \end{bmatrix}^T \\
\mathbf{x}_{k+1} = \mathbf{F}_k \mathbf{x}_k + \mathbf{G}_k \mathbf{u}_k, \mathbf{y}_k = \mathbf{H}\mathbf{x}_k
\end{gathered} \tag{24}
$$

where $\mathbf{F}_k$, $\mathbf{G}_k$, and $\mathbf{H}$ are the matrices of a discrete space state form. In this study, a third-order 5 Hz Butterworth low-pass filter was used to remove noise from the signal. Because the Kalman filter operates at 100 Hz, it was possible to discretize it as in (25) through the zero-order hold technique.

$$
\begin{gathered}
\mathbf{F}_k = \mathbf{I} + \mathbf{A}(v_x(k), F_{zi}(k), \theta_k)\Delta t, \\
\mathbf{G}_k = \mathbf{B}(v_x(k), F_{zi}(k), \theta_k)\Delta t, \mathbf{H} = \mathbf{C}
\end{gathered} \tag{25}
$$

where Δt is the sampling time of the Kalman filter and its value is $10\,ms$. The discrete-time system was a linear time-varying (LTV) system that includes velocity (v_x) and normal force (F_{zi}). It is also affected by the cornering stiffness parameter (θ).

- Initialization

$$\begin{aligned}\hat{\theta}_0 &= E[\theta],\ \mathbf{P}_{\theta,0} = E[(\theta-\hat{\theta}_0)(\theta-\hat{\theta}_0)^T]\\ \hat{\mathbf{x}}_0 &= E[\mathbf{x}_0],\ \mathbf{P}_{\mathbf{x},0} = E[(\mathbf{x}_0-\hat{\mathbf{x}}_0)(\mathbf{x}_0-\hat{\mathbf{x}}_0)^T]\end{aligned} \tag{26}$$

- Parameter prediction

$$\hat{\theta}_k^- = \hat{\theta}_{k-1}, \mathbf{P}_{\theta,k}^- = \mathbf{P}_{\theta,k-1} + \mathbf{Q}_\theta \tag{27}$$

Here, the covariance matrix $\mathbf{Q}_\theta$ determines how fast the parameter changes. In proportion to the scale of the parameter, it was set as follows:

$$\mathbf{Q}_\theta = \Delta t \begin{bmatrix} 10^{-3} & 0 \\ 0 & 10^{-14} \end{bmatrix} \tag{28}$$

- State prediction

$$\begin{aligned}\hat{\mathbf{x}}_k^- &= \mathbf{F}_k\Big|_{\theta=\hat{\theta}_k^-}\hat{\mathbf{x}}_{k-1} + \mathbf{G}_k\Big|_{\theta=\hat{\theta}_k^-}\mathbf{u}_k\\ \mathbf{P}_{\mathbf{x},k}^- &= \mathbf{F}_k\Big|_{\theta=\hat{\theta}_k^-}\mathbf{P}_{\mathbf{x},k-1}\mathbf{F}_k\Big|_{\theta=\hat{\theta}_k^-}^T + \mathbf{Q}_\mathbf{x}\end{aligned} \tag{29}$$

By analyzing the model uncertainty, the covariance matrix $\mathbf{Q}_\mathbf{x}$ was set as in (30). In addition, because the bicycle model and the linear tire model were used in this study, the uncertainty of the model will increase with the increase of longitudinal and lateral acceleration. Therefore, the acceleration term was introduced in the covariance matrix. This serves to make estimation of the state more reliant on the measurements than on the model when the longitudinal and lateral accelerations are large.

$$\begin{aligned}\mathbf{Q}_\mathbf{x} = \Delta t &\begin{bmatrix} 10^{-4} & 0 & 0 & 0 \\ 0 & 10^{-4} & 0 & 0 \\ 0 & 0 & 10^{-4} & 0 \\ 0 & 0 & 0 & 10^{-4} \end{bmatrix}\\ \times &\left(1 + \frac{\sqrt{a_{x1}^2 + a_{y1}^2} + \sqrt{a_{x2}^2 + a_{y2}^2}}{2}\right)\end{aligned} \tag{30}$$

- State correction

$$\begin{aligned}\mathbf{K}_{\mathbf{x},k} &= \mathbf{P}_{\mathbf{x},k}^-\mathbf{H}^T(\mathbf{H}\mathbf{P}_{\mathbf{x},k}^-\mathbf{H}^T + \mathbf{R}_\mathbf{x})^{-1}\\ \hat{\mathbf{x}}_k &= \hat{\mathbf{x}}_k^- + \mathbf{K}_{\mathbf{x},k}(\mathbf{y}_k - \mathbf{H}\hat{\mathbf{x}}_k^-)\\ \mathbf{P}_{\mathbf{x},k} &= (\mathbf{I} - \mathbf{K}_{\mathbf{x},k}\mathbf{H})\mathbf{P}_{\mathbf{x},k}^-\end{aligned} \tag{31}$$

Matrix $\mathbf{R}_\mathbf{x}$ is the noise covariance matrix of the measurements. Through noise analysis of the sensor used, $\mathbf{R}_\mathbf{x}$ was set as follows:

$$\mathbf{R}_\mathbf{x} = \frac{1}{\Delta t}\begin{bmatrix} 0.5\times10^{-4} & 0 & 0 \\ 0 & 0.5\times10^{-4} & 0 \\ 0 & 0 & 0.5\times10^{-4} \end{bmatrix} \tag{32}$$

- Parameter correction

$$\begin{aligned}\mathbf{K}_{\theta,k} &= \mathbf{P}_{\theta,k}^-\mathbf{H}_{\theta,k}^T(\mathbf{H}_{\theta,k}\mathbf{P}_{\theta,k}^-\mathbf{H}_{\theta,k}^T + \mathbf{R}_\theta)^{-1}\\ \hat{\theta}_k &= \hat{\theta}_k^- + \mathbf{K}_{\theta,k}(\mathbf{y}_k - \mathbf{H}\hat{\mathbf{x}}_k^-)\\ \mathbf{P}_{\theta,k} &= (\mathbf{I} - \mathbf{K}_{\theta,k}\mathbf{H}_{\theta,k})\mathbf{P}_{\theta,k}^-\end{aligned} \tag{33}$$

Because the state Kalman filter and parameter Kalman filter use the same measurement, the covariance matrices are the same ($\mathbf{R}_\theta = \mathbf{R}_\mathbf{x}$). Matrix $\mathbf{H}_{\theta,k}$ means output residual due to parameter errors. It can be simplified as follows:

$$\begin{aligned}\mathbf{H}_{\theta,k} &= \mathbf{H}\frac{\partial\hat{\mathbf{x}}_k^-}{\partial\theta}\Big|_{\theta=\hat{\theta}_k^-}\\ &= \mathbf{H}\left[\frac{\partial\mathbf{F}_k}{\partial\mathbf{a}}\hat{\mathbf{x}}_{k-1} + \frac{\partial\mathbf{G}_k}{\partial\mathbf{a}}\mathbf{u}_k\ \frac{\partial\mathbf{F}_k}{\partial\mathbf{b}}\hat{\mathbf{x}}_{k-1} + \frac{\partial\mathbf{G}_k}{\partial\mathbf{b}}\mathbf{u}_k\right]\Big|_{\theta=\hat{\theta}_k^-}\end{aligned} \tag{34}$$

Through the proposed dual LTV Kalman filter, the state and parameters of the articulated vehicle were estimated simultaneously. Finally, the sideslip angle and the cornering stiffness were estimated as follows:

$$\begin{aligned}\hat{\beta}_1 &= \frac{\hat{v}_{y1}}{v_x}\\ \hat{\beta}_2 &= \frac{\hat{v}_{y1}}{v_x} - \hat{\alpha} - \frac{(l_{r1}+P_1)\hat{r}_1 + l_{f2}\hat{r}_2}{v_x}\\ \hat{C}_i &= \hat{a}\hat{F}_{zi} - \hat{b}\hat{F}_{zi}^2\end{aligned} \tag{35}$$

3.2. Observability of the proposed estimation algorithm

The observability of the system determines the estimation performance and stability of observers, including the Kalman filter [38]. If the observability of the system is guaranteed, the convergence of the estimator is also guaranteed. Therefore, in this section, the observability of the proposed estimation algorithm is analyzed using the observability matrix. The following statements about the observability matrix are widely known [38].

- For a Kalman filter, a system with state vector $\mathbf{x}$ of dimension n is observable if the observability matrix ($\mathbf{O}$) has row rank n.

The observability matrices of the state Kalman filter and the parameter Kalman filter were both analyzed.

- Observability of the state Kalman filter

For the state Kalman filter, the observability matrix and rank are expressed as follows:

$$\mathbf{O}_\mathbf{x} = \begin{bmatrix}\mathbf{H} & \mathbf{H}\mathbf{F}_k & \mathbf{H}\mathbf{F}_k^2 & \mathbf{H}\mathbf{F}_k^3\end{bmatrix}, rank(\mathbf{O}_\mathbf{x}) = 4 \tag{36}$$

where $\mathbf{O}_\mathbf{x}$ is the observability matrix of the state Kalman filter. All states were observable because the number of states matched the rank of the observability matrix.

- Observability of the parameter Kalman filter

The stability of the parameter Kalman filter was also verified through the observability matrix. Because the parameter does not change at the prediction stage, the observability matrix and its rank are expressed as follows:

$$\mathbf{O}_\theta = \mathbf{H}_{\theta,\mathbf{k}}, rank(\mathbf{O}_\theta) = 2 \tag{37}$$

where $\mathbf{O}_\theta$ is the observability matrix of the parameter Kalman filter. The rank of the observability matrix of the parameter Kalman filter matched the number of parameters to be estimated. This means that all parameters are observable and that estimation stability is guaranteed. If the cornering stiffness of each axle has to be estimated individually, observability is not guaranteed. This is because, although the observability matrix rank is 2, the number of estimated parameters is 3. In this study, the cornering stiffness of each axis was expressed using two cornering stiffness parameters as shown in (9). Reducing the number of parameters ensures the observability of the parameter Kalman filter.

In this section, the dual LTV Kalman filter was proposed for estimating simultaneously the sideslip angle and cornering stiffness. The stability of the proposed estimation algorithm was verified using its observability matrix. The proposed algorithm has advantages in terms of computation time and robustness.

4. SIMULATION RESULTS

4.1. Simulation environment

The simulation was conducted to analyze the performance of the proposed algorithm for various situations that are difficult to implement in actual experiments. The proposed algorithm performance was verified through simulation using TruckSim as shown in Fig. 10 (a). In the simulation, the specifications of the articulated vehicle were the same as in the experiment. Noise with a signal-to-noise ratio of 5 % was added to the sensor signal. A third-order Butterworth low-pass filter was used to filter out the noise.

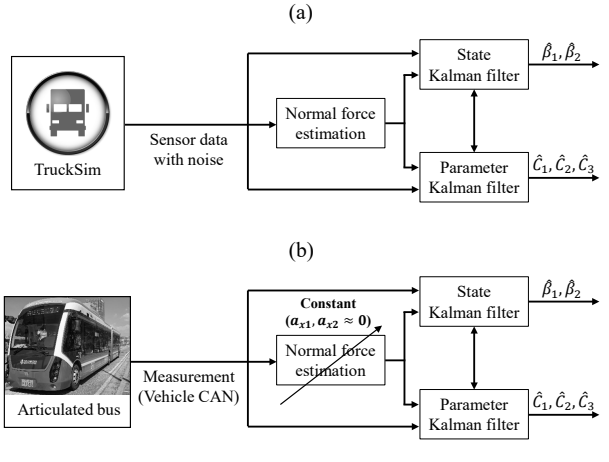

Figure 10: Block diagram: (a) Simulations (b) Experiments

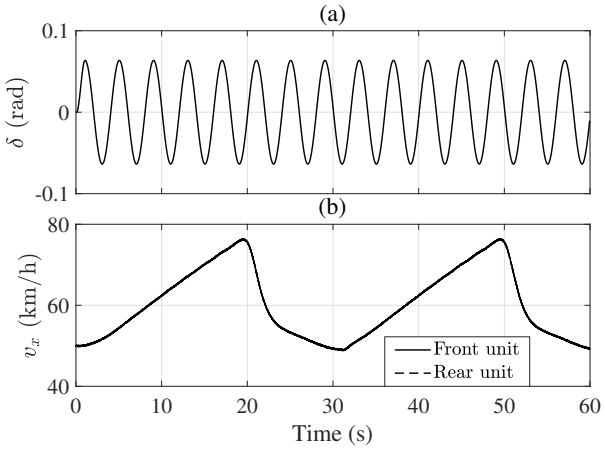

Figure 11: Simulation scenario (sine steer, various acceleration and road surface): (a) Steering angle of the first axle (b) Velocity of the front unit and rear unit

As a simulation scenario, sine steer with deceleration and acceleration was selected. The sine steer scenario uses a sine function to steer. We verified the robustness of the proposed algorithm through sine steer with acceleration and deceleration. The steering angle and longitudinal velocity of the front unit and rear unit of the scenario are as shown in Fig. 11. Longitudinal acceleration and lateral acceleration in the simulation are as shown in Fig. 12 (a). In addition, to evaluate the robustness of the estimation algorithm according to road surface changes, the tire-road friction coefficient (μ) was set to 1.0 from 0 to 30 sec and then set to 0.5 after 30 sec.

Because the cornering stiffness can change up to 50 % depending on the road surface, 150 % and 50 % of the true cornering stiffness were set as the initial cornering stiffness. In Figs. 13 and 14, solid lines, dash-dotted lines, and dashed lines represent the true value, and the estimated values for the 150 % and 50 % initial cornering stiffness, respectively. Estimation performance was analyzed using RMS error for the sideslip angle and the final error for cornering stiffness. In addition, the extended Kalman filter was introduced as an algorithm to compare with the dual LTV Kalman filter. The extended Kalman filter is provided in Appendix A. In Figs. 13 and 14, blue lines and red lines show the estimation results through the dual LTV Kalman filter (DKF) and extended Kalman filter (EKF), respectively.

4.2. Simulation results: Sine steer with varying acceleration and road surface

The estimated sideslip angle of the first and rear units is shown in Fig. 12. The estimated cornering stiffness of each axle is shown in Fig. 13. The estimation performance is shown in Tables 3 and 4.

At the beginning of the sideslip estimation, as shown in Fig. 12, the estimation performance of the sideslip angle error was not good because of cornering stiffness error. However, as the cornering stiffness converged to the real

Table 3
Estimation error of sideslip angle (RMS error) and cornering stiffness (final error), $\mu = 1.0$ (0 ~ 30 seconds).

Error	DKF		EKF	
	$0.5 \times C_{true}$	$1.5 \times C_{true}$	$0.5 \times C_{true}$	$1.5 \times C_{true}$
β_1 (rad)	2.61E-03	2.59E-03	2.67E-03	2.72E-03
β_2 (rad)	3.43E-03	3.70E-03	3.18E-03	3.85E-03
C_1 (%)	-2.05	-1.29	-3.63	4.55
C_2 (%)	5.77	5.79	4.65	8.64
C_3 (%)	1.25	1.82	-0.21	6.93

value, the sideslip angle error decreased also. Estimated sideslip angles of the first and rear units had a phase lag effect. This is because the Kalman filter acts as a low-pass filter. In addition, we verified that the proposed algorithm was guaranteed to have good performance even with longitudinal acceleration and mu changes. Compared with the EKF algorithm, the proposed DKF algorithm had similarly or slightly better sideslip angle estimation performance. For estimation error, DKF had an RMS error of $3.07E-03\,rad$, EKF had an RMS error of $3.15E-03\,rad$ on average. These indicate an error of approximately $0.18\,deg$.

Estimation results for cornering stiffness are as shown in Fig. 14, and Tables 3 and 4 show the estimated performance of the two areas according to μ. As a result of estimation using the DKF and EKF algorithms, the cornering stiffness of the three axles converged to the true value. The longitudinal acceleration was greatest at about $20sec$ and $50sec$, respectively the estimated cornering stiffness values also oscillated. As such, because the linear tire model was used in this study, the estimation performance may deteriorate when large longitudinal acceleration is applied. Moreover, the true cornering stiffness decreases as the μ changes after $30\,sec$. Accordingly, the estimated cornering stiffness value also converges to a smaller value. As shown in Fig. 14, DKF responds faster than EKF when the parameters change over time. For the entire simulation and all axes, the average estimation error of DKF was 3.03 % and that of EKF was 5.70 %.

In Section 4, the performance of the proposed sideslip angle and the cornering stiffness estimation algorithm was verified through simulation using TruckSim. The proposed algorithm for estimation of the sideslip angle and cornering stiffness showed good performance even for various mu and longitudinal accelerations. Moreover, the proposed DKF had slightly better performance and shorter computation time than EKF did, as shown in Table 5. In addition, C_i was observed to change according to μ. In future studies, it is expected that it will be possible to estimate μ based on the estimate of C_i.

Table 4
Estimation error of sideslip angle (RMS error) and cornering stiffness (final error), $\mu = 0.5$ (30 ~ 60 seconds).

Error	DKF		EKF	
	$0.5 \times C_{true}$	$1.5 \times C_{true}$	$0.5 \times C_{true}$	$1.5 \times C_{true}$
β_1 (rad)	2.72E-03	2.71E-03	2.69E-03	2.89E-03
β_2 (rad)	3.42E-03	3.43E-03	3.41E-03	3.80E-03
C_1 (%)	0.82	-0.91	5.13	8.68
C_2 (%)	7.10	7.13	8.62	10.34
C_3 (%)	-1.25	-1.19	2.13	5.05

Table 5
Computation time of estimation algorithms.

	DKF	EKF
Time (sec)	5.2548E-05	5.9426E-05

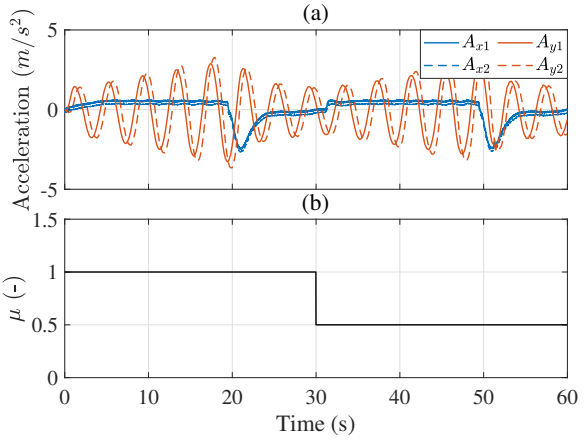

Figure 12: Simulation scenario (sine steer, various acceleration and road surface): (a) Longitudinal and lateral acceleration of the front unit and rear unit (b) Tire–road friction coefficient

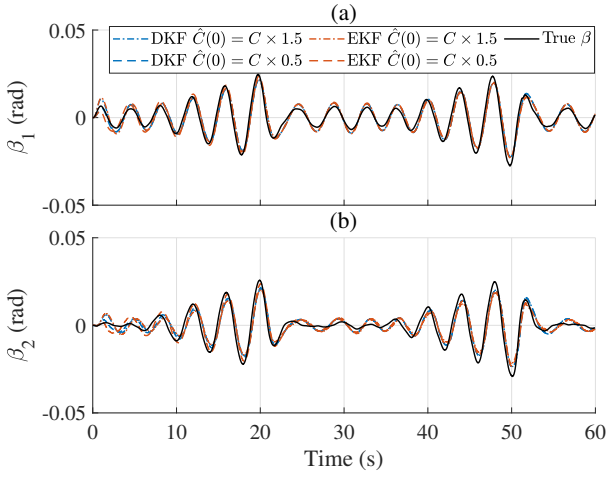

Figure 13: Simulation results from estimating the sideslip angle: (a) Sideslip angle of the front unit (b) Sideslip angle of the rear unit

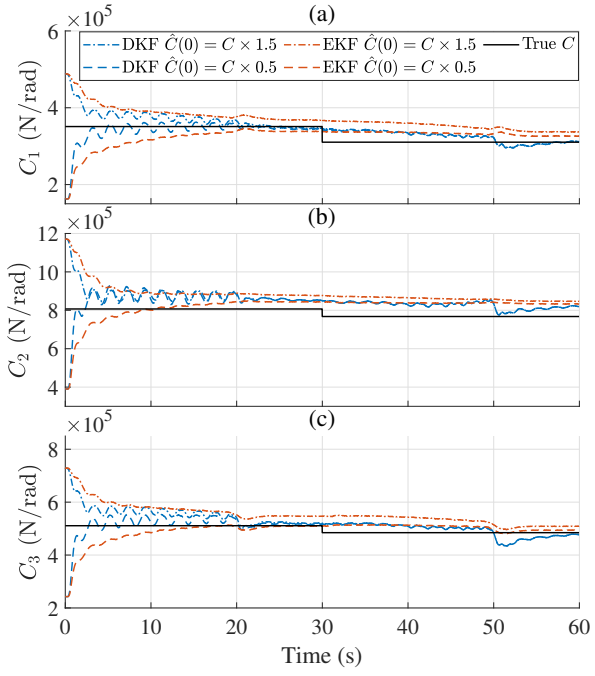

Figure 14: Simulation results from estimating the cornering stiffness: (a) First axle cornering stiffness (b) Second axle cornering stiffness (c) Third axle cornering stiffness

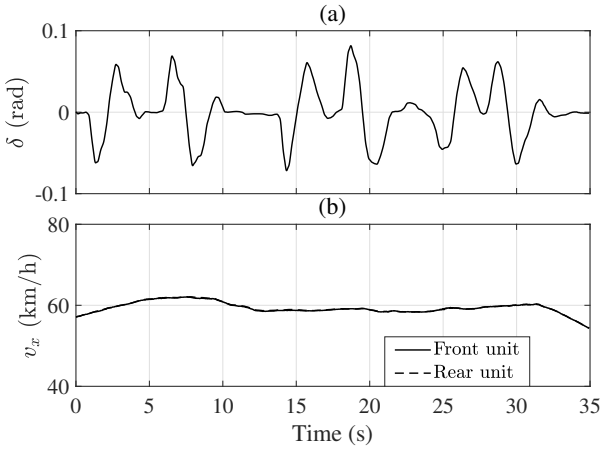

Figure 15: Experimental scenario (three DLCs): (a) Steering angle of the first axle (b) Velocity of the front unit and rear unit

Table 6
Estimation error of sideslip angle (RMS error) and cornering stiffness (final error), $\mu = 0.5$ (30 ~ 60 seconds).

Error	DKF		EKF	
	$0.5 \times C_{true}$	$1.5 \times C_{true}$	$0.5 \times C_{true}$	$1.5 \times C_{true}$
β_1 (rad)	4.69E-03	4.20E-03	4.73E-03	4.07E-03
β_2 (rad)	2.97E-03	2.49E-03	3.20E-03	2.70E-03
C_1 (%)	-9.70	-0.34	-6.03	15.53
C_2 (%)	-2.73	-0.81	-1.85	4.38
C_3 (%)	-8.52	-0.98	-5.25	12.29

5. EXPERIMENTAL RESULTS

5.1. Experimental setup

The proposed estimation algorithm was verified through experiments performed using an articulated bus called a bi-modal tram [39], as shown in Fig. 1. The specifications of the articulated bus are given in Table 1. In the experimental setup, vehicle controller area network (CAN) data were used as system measurements as shown in Fig. 10 (b). A third-order, 5 Hz Butterworth low-pass filter was used for noise filtering. The reference signals were acquired by the RT-3000. Two RT-3000s were used, one attached to the front unit and one to the rear unit of the articulated bus. The purpose of the experiment was to verify the performance of estimating the sideslip angle and cornering stiffness. In this section, the results from estimation of the sideslip angle and cornering stiffness are presented.

Double lane change (DLC) was chosen as the experimental scenario. The DLC is a situation in which the lane is changed rapidly twice to avoid obstacles. It is also an important situation in terms of obstacle avoidance in autonomous driving. Accurate vehicle states and parameters are essential to follow the desired path without losing control or becoming unsafe during the violent lateral movements.

For the experiments, it was difficult to verify the load transfer model due to the absence of equipment to measure the normal force of each axis. Therefore, to neglect load transfer, the longitudinal velocity was fixed at 60 km/h as much as possible. In conclusion, because the load transfer model was verified through simulation, experiments were performed to determine the pure sideslip angle without longitudinal acceleration. The longitudinal velocity and the front wheel steering angles are shown in Fig. 15.

As with the simulation, 150 % and 50 % of the actual cornering stiffness were set as the initial cornering stiffness. Similarly, notations of the lines in Figs. 16 and 17 are the same as in Figs. 13 and 14. The estimation performance was analyzed using the RMS error for the sideslip angle, and the final estimation error for the cornering stiffness.

5.2. Experimental results: 60km/h DLC

The estimated values and estimation performance for the sideslip angles are shown in Fig. 16 and Table 6. A sideslip angle estimation error occurs at the beginning due to the cornering stiffness error, but after the cornering stiffness converges to the true value, the sideslip angle shows good estimation performance. The average estimation errors of the sideslip angles of the proposed DKF and EKF are $3.53E-03\,rad$ and $3.68E-03\,rad$, respectively. The error for each of these is approximately $0.20\,deg$.

The estimated cornering stiffness value and performance in the DLC scenario are shown in Fig. 17 and Table 6. As shown in Fig. 17, the cornering stiffness quickly converges to the true value at the beginning of the first lane change. The

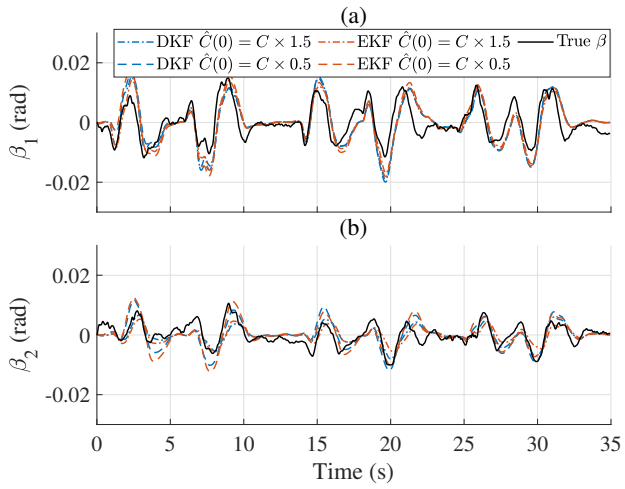

Figure 16: Experimental results from estimating the sideslip angle: (a) Sideslip angle of the front unit (b) Sideslip angle of the rear unit

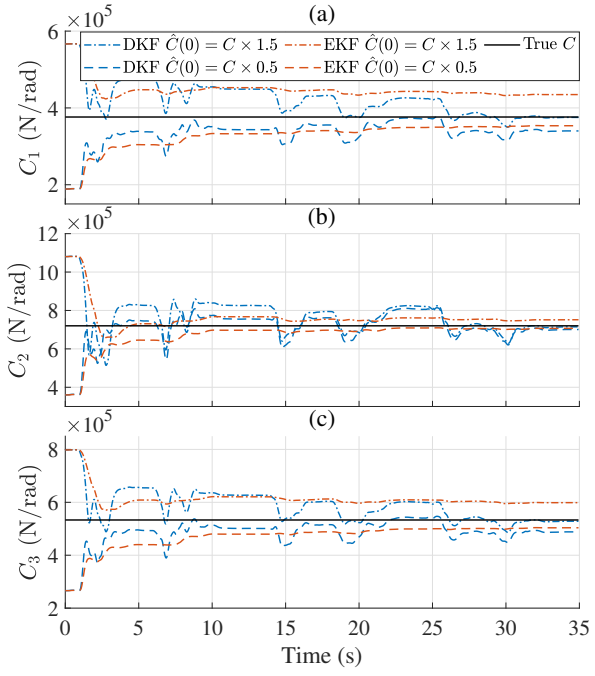

Figure 17: Experimental results from estimating the cornering stiffness: (a) First axle cornering stiffness (b) Second axle cornering stiffness (c) Third axle cornering stiffness

fast convergence speed is an advantage for obstacle avoidance in autonomous driving. For the proposed DKF and EKF, the average estimation errors of cornering stiffness are 3.85 % and 7.56 %, respectively. In addition, the computation time of each algorithm had the same value as the simulation. The proposed DKF was better in terms of computation time and estimation performance.

The performance of the proposed estimation algorithm was verified by performing an experiment using an articulated bus. Some estimation errors occurred. These were analyzed and found to be due to model uncertainty, measurement noise, and specification errors. Nevertheless, the sideslip angle and cornering stiffness were estimated with sufficient accuracy for vehicle control. In conclusion, it was verified experimentally that the proposed estimation algorithm simultaneously estimated sideslip angle and cornering stiffness with high accuracy.

6. CONCLUSION

In this paper, we presented a strategy for estimating the sideslip angle and cornering stiffness of articulated vehicles. A constrained lateral dynamics model was proposed and used in the estimation algorithm. The sideslip angle and cornering stiffness were estimated simultaneously using a dual LTV Kalman filter. This paper makes two major contributions. First, unlike previous complex articulated vehicle models, a constrained model was proposed that uses physical constraints. The proposed model describes the lateral dynamics of articulated vehicles with only four states. It has an advantage in terms of stability, calibration issues, and computational time. Second, the sideslip angle and cornering stiffness were estimated simultaneously using a dual LTV Kalman filter. Moreover, estimation stability was guaranteed by using its observability matrix. The proposed estimation algorithm was verified through simulations and by performing experiments using an articulated bus. The estimation performance was accurate enough for use in vehicle control applications. The proposed model and estimation algorithm are expected to contribute to the field of vehicle safety control and autonomous driving.

Although the proposed algorithm demonstrates good estimation performance for sideslip angle and cornering stiffness, there are some limitations. For example, the bicycle model was used to describe articulated vehicles. This does not allow consideration of pitch and roll dynamics. High degrees-of-freedom modeling will be required to overcome this. However, using complex models comes with poor observability and demanding computation issues. In future work, selecting an appropriate model will be the first assignment. In addition, the tire force was modeled using a linear tire model. Therefore, the proposed algorithm cannot cope effectively with the combined slip situation. This leads to the degradation of estimation performance under severe driving conditions. Therefore, future work will include nonlinear tire modeling to describe the combined slip effect. This should be accompanied by estimation of states and parameters accordingly. The incorporation of longitudinal dynamics models could ensure observability. We will work to overcome the limitations and advance the model. This study provides a cornerstone for higher-level modeling of articulated vehicles and estimation of their states and parameters.

Acknowledgment

This research was partly supported by the grant(21TLRP-C152499-03) from Transportation & Logistics Research Program funded by Ministry of Land, Infrastructure and Transport(MOLIT) of Korea government and Korea Agency for Infrastructure Technology Advancement(KAIA)., the BK21 FOUR Program of the National Research Foundation Korea(NRF) grant funded by the Ministry of Education(MOE)., the National Research Foundation of Korea(NRF) grant funded by the Korea government(MSIP) (No. 2020R1A2B5B01001531)., the Technology Innovation Program (20014983, Development of autonomous chassis platform for a modular vehicle) funded By the Ministry of Trade, Industry & Energy(MOTIE, Korea)., and the Technology Innovation Program (20010263, Development of innovative design for UX environment improvement and commercialization model of wheelchair electric motorization kit with enhanced portability and convenience) funded By the Ministry of Trade, Industry & Energy(MOTIE, Korea).

A. Extended Kalman filter

The extended Kalman filter estimates augmented states that combine states and parameters. The symbols are the same as in Section 3.1.

- Discretization of system dynamics

$$\begin{gathered}\text{Let, } \bar{\mathbf{x}}_k = \begin{bmatrix}\mathbf{x}_k \\ \theta_k\end{bmatrix}, \mathbf{u}_k = \delta(k), \mathbf{y}_k = \begin{bmatrix} r_1(k) \; r_2(k) \; \alpha(k)\end{bmatrix}^T, \\ \mathbf{x}_k = \begin{bmatrix} v_{y1}(k) \; r_1(k) \; r_2(k) \; \alpha(k)\end{bmatrix}^T, \theta_k = \begin{bmatrix} a(k) \; b(k)\end{bmatrix}^T \\ \bar{\mathbf{x}}_{k+1} = f_k(\bar{\mathbf{x}}_k, \mathbf{u}_k) = \begin{bmatrix}\mathbf{F}_k\mathbf{x}_k + \mathbf{G}_k\mathbf{u}_k \\ \mathbf{0}_{2\times1}\end{bmatrix}, \\ \mathbf{y}_k = \bar{\mathbf{H}}\mathbf{x}_k = \begin{bmatrix}\mathbf{H} \; \mathbf{0}_{3\times2}\end{bmatrix}\bar{\mathbf{x}}_k\end{gathered} \tag{38}$$

- Initialization

$$\hat{\bar{\mathbf{x}}}_0 = \begin{bmatrix}\hat{\mathbf{x}}_0 \\ \hat{\theta}_0\end{bmatrix}, \mathbf{P}_{\bar{\mathbf{x}},0} = \begin{bmatrix}\mathbf{P}_{\mathbf{x},0} & \mathbf{0}_{4\times2} \\ \mathbf{0}_{2\times4} & \mathbf{P}_{\theta,0}\end{bmatrix} \tag{39}$$

- State prediction

$$\begin{gathered}\hat{\bar{\mathbf{x}}}_k^- = f_k(\hat{\bar{\mathbf{x}}}_{k-1}, \mathbf{u}_k), \mathbf{P}_{\bar{\mathbf{x}},k}^- = \bar{\mathbf{F}}_k\mathbf{P}_{\bar{\mathbf{x}},k-1}\bar{\mathbf{F}}_k^T + \mathbf{Q}_{\bar{\mathbf{x}}} \\ \text{where } \bar{\mathbf{F}}_k = \frac{\partial f_k(\bar{\mathbf{x}}_k, \mathbf{u}_k)}{\partial\bar{\mathbf{x}}}\Big|_{\bar{\mathbf{x}}=\hat{\bar{\mathbf{x}}}_k^-}, \mathbf{Q}_{\bar{\mathbf{x}}} = \begin{bmatrix}\mathbf{Q}_{\mathbf{x}} & \mathbf{0}_{4\times2} \\ \mathbf{0}_{2\times4} & \mathbf{Q}_\theta\end{bmatrix}\end{gathered} \tag{40}$$

- State correction

$$\begin{gathered}\mathbf{K}_{\bar{\mathbf{x}},k} = \mathbf{P}_{\bar{\mathbf{x}},k}^-\bar{\mathbf{H}}^T(\bar{\mathbf{H}}\mathbf{P}_{\bar{\mathbf{x}},k}^-\bar{\mathbf{H}}^T + \mathbf{R}_{\bar{\mathbf{x}}})^{-1} \\ \hat{\bar{\mathbf{x}}}_k = \hat{\bar{\mathbf{x}}}_k^- + \mathbf{K}_{\bar{\mathbf{x}},k}(\mathbf{y}_k - \bar{\mathbf{H}}\hat{\bar{\mathbf{x}}}_k^-) \\ \mathbf{P}_{\bar{\mathbf{x}},k} = (\mathbf{I} - \mathbf{K}_{\bar{\mathbf{x}},k}\bar{\mathbf{H}})\mathbf{P}_{\bar{\mathbf{x}},k}^- \\ \text{where } \bar{\mathbf{H}} = \begin{bmatrix}\mathbf{H} \; \mathbf{0}_{3\times2}\end{bmatrix}, \mathbf{R}_{\bar{\mathbf{x}}} = \mathbf{R}_{\mathbf{x}}\end{gathered} \tag{41}$$

References

[1] F. Bu, H.-S. Tan, J. Huang, Lateral control of an articulated bus for lane guidance and curbside precision docking, in: Proceedings of the 2010 American Control Conference, IEEE, 2010, pp. 3854–3859.

[2] Y. Zhang, A. Khajepour, Y. Huang, Multi-axle/articulated bus dynamics modeling: a reconfigurable approach, Vehicle System Dynamics 56 (2018) 1315–1343.

[3] S. Oikawa, Y. Matsui, N. Kubota, S. Aomura, K. Sorimachi, A. Imanishi, T. Fujimura, Features of fatal truck accidents compared with sedans, International journal of automotive technology 22 (2021) 931–939.

[4] A. Reński, Investigation of the influence of the centre of gravity position on the course of vehicle rollover, in: Proceedings of the 24th International Technical Conference on the Enhanced Safety of Vehicles (ESV) National Highway Traffic Safety Administration, Gothenburg, Sweden, 2015, pp. 8–11.

[5] D. J. Sampson, D. Cebon, Achievable roll stability of heavy road vehicles, Proceedings of the Institution of Mechanical Engineers, Part D: Journal of Automobile Engineering 217 (2003) 269–287.

[6] R. Dehghani, H. Khanlo, J. Fakhraei, Active chaos control of a heavy articulated vehicle equipped with magnetorheological dampers, Nonlinear Dynamics 87 (2017) 1923–1942.

[7] Y.-C. Kim, K.-H. Yun, K.-D. Min, Y.-S. Byun, J.-K. Mok, A lateral dynamic model of an all wheel steered bimodal vehicle, in: 2007 International Conference on Control, Automation and Systems, IEEE, 2007, pp. 1734–1737.

[8] M. Abroshan, R. Hajiloo, E. Hashemi, A. Khajepour, Model predictive-based tractor-trailer stabilisation using differential braking with experimental verification, Vehicle system dynamics 59 (2021) 1190–1213.

[9] A. Habibnejad Korayem, E. Hashemi, A. Khajepour, B. Fidan, Estimation of vehicle-trailer hitch-forces and lateral tire forces independent of trailer type and geometry, Journal of Dynamic Systems, Measurement, and Control (2022).

[10] D. Chindamo, B. Lenzo, M. Gadola, On the vehicle sideslip angle estimation: a literature review of methods, models, and innovations, applied sciences 8 (2018) 355.

[11] J. Liu, Z. Wang, L. Zhang, P. Walker, Sideslip angle estimation of ground vehicles: a comparative study, IET Control Theory and Applications (2020).

[12] D. Selmanaj, M. Corno, G. Panzani, S. M. Savaresi, Vehicle sideslip estimation: A kinematic based approach, Control Engineering Practice 67 (2017) 1–12.

[13] X. Ding, Z. Wang, L. Zhang, Event-triggered vehicle sideslip angle estimation based on low-cost sensors, IEEE Transactions on Industrial Informatics (2021).

[14] T. Gräber, S. Lupberger, M. Unterreiner, D. Schramm, A hybrid approach to side-slip angle estimation with recurrent neural networks and kinematic vehicle models, IEEE Transactions on Intelligent Vehicles 4 (2018) 39–47.

[15] J.-H. Yoon, H. Peng, Robust vehicle sideslip angle estimation through a disturbance rejection filter that integrates a magnetometer with gps, IEEE Transactions on Intelligent Transportation Systems 15 (2013) 191–204.

[16] G. Park, S. B. Choi, D. Hyun, J. Lee, Integrated observer approach using in-vehicle sensors and gps for vehicle state estimation, Mechatronics 50 (2018) 134–147.

[17] M. Doumiati, A. C. Victorino, A. Charara, D. Lechner, Onboard real-time estimation of vehicle lateral tire–road forces and sideslip angle, IEEE/ASME Transactions on Mechatronics 16 (2010) 601–614.

[18] W. Wenkang, F. Jingan, S. Bao, L. Xinxin, Vehicle state estimation using interacting multiple model based on square root cubature kalman filter, Applied Sciences 11 (2021) 10772.

[19] M. Jalali, E. Hashemi, A. Khajepour, S.-k. Chen, B. Litkouhi, Integrated model predictive control and velocity estimation of electric vehicles, Mechatronics 46 (2017) 84–100.

[20] R. Chumsamutr, T. Fujioka, M. Abe, Sensitivity analysis of side-slip angle observer based on a tire model, Vehicle system dynamics 44

(2006) 513–527.
[21] B. Li, C. Huang, Y. Wu, B. Zhang, H. Du, A three-dimensional integrated non-linear coordinate control framework for combined yaw-and roll-stability control during tyre blow-out, Sensors 21 (2021) 8328.
[22] M. Choi, J. J. Oh, S. B. Choi, Linearized recursive least squares methods for real-time identification of tire–road friction coefficient, IEEE Transactions on Vehicular Technology 62 (2013) 2906–2918.
[23] C. Sierra, E. Tseng, A. Jain, H. Peng, Cornering stiffness estimation based on vehicle lateral dynamics, Vehicle System Dynamics 44 (2006) 24–38.
[24] G. Baffet, A. Charara, D. Lechner, Estimation of vehicle sideslip, tire force and wheel cornering stiffness, Control Engineering Practice 17 (2009) 1255–1264.
[25] R. Anderson, D. M. Bevly, Estimation of tire cornering stiffness using gps to improve model based estimation of vehicle states, in: IEEE Proceedings. Intelligent Vehicles Symposium, 2005., IEEE, 2005, pp. 801–806.
[26] C. Cheng, D. Cebon, Parameter and state estimation for articulated heavy vehicles, Vehicle System Dynamics 49 (2011) 399–418.
[27] A. Nikoofard, F. R. Salmasi, A. K. Sedigh, An adaptive observer for linear systems with reduced adaptation laws and measurement faults, in: 2011 Chinese Control and Decision Conference (CCDC), IEEE, 2011, pp. 1105–1109.
[28] Q. Zhang, Adaptive observer for multiple-input-multiple-output (mimo) linear time-varying systems, IEEE transactions on automatic control 47 (2002) 525–529.
[29] R. Bao, M. Jia, E. Sabbioni, H. Yu, et al., Vehicle state and parameter estimation under driving situation based on extended kalman particle filter method (2015).
[30] X. Jin, G. Yin, Estimation of lateral tire–road forces and sideslip angle for electric vehicles using interacting multiple model filter approach, Journal of the Franklin Institute 352 (2015) 686–707.
[31] T. A. Wenzel, K. Burnham, M. Blundell, R. Williams, Dual extended kalman filter for vehicle state and parameter estimation, Vehicle system dynamics 44 (2006) 153–171.
[32] Y. Liu, X. Ji, K. Yang, X. He, X. Na, Y. Liu, Finite-time optimized robust control with adaptive state estimation algorithm for autonomous heavy vehicle, Mechanical Systems and Signal Processing 139 (2020) 106616.
[33] C. J. Backi, J. T. Gravdahl, S. Skogestad, Ifac journal of systems and control (2020).
[34] R. Rajamani, Vehicle dynamics and control, Springer Science & Business Media, 2011.
[35] H. B. Pacejka, E. Bakker, The magic formula tyre model, Vehicle system dynamics 21 (1992) 1–18.
[36] D. Jeong, S. B. Choi, J. Lee, M. Kim, H. Lee, Tire dimensionless numbers for analysis of tire characteristics and intelligent tire signals, Mechanical Systems and Signal Processing 161 (2021) 107927.
[37] S. Haykin, Kalman filtering and neural networks, volume 47, John Wiley & Sons, 2004.
[38] D. Simon, Optimal state estimation: Kalman, H infinity, and nonlinear approaches, John Wiley & Sons, 2006.
[39] W. S. Jang, J. Kim, B. A. Engel, S. W. Kang, Y. Park, H. Yoon, K. J. Lim, Y. Jung, Y. Shin, Development of a prototype web gis-based disaster management system for safe operation of the next generation bimodal tram, south korea—focused flooding and snowfall, Sustainability 6 (2014) 1776–1795.

Dasol Jeong received the B.S. degree in mechanical engineering from Korea Advanced Institute of Science and Technology (KAIST), Deajeon, Korea, and M.S. in Mechanical Engineering from the Korea Advanced Institute of Science and Technology KAIST, in 2017 and 2019, respectively. Since 2019, he is currently pursuing the Ph.D. degree in Mechanical engineering at KAIST. His research interests include vehicle dynamics and control, intelligent tires and control theory.

Geonhee Ko received the B.S. degree in mechanical engineering from Korea Advanced Institute of Science and Technology (KAIST), Daejeon, Korea, in 2019. Since 2019, he is working toward the M.S. degree in Mechanical engineering at KAIST. He is currently a Researcher with the Automotive Control Laboratory, Department of Mechanical Engineering, KAIST. His research interests include vehicle dynamics and control, vehicle vibration and system identification.

Seibum B. Choi received the B.S. in mechanical engineering from Seoul National University, Seoul, Korea, the M.S. in mechanical engineering from KAIST, Deajeon, Korea, and the Ph.D. in control from the University of California, Berkeley, CA, USA, in 1993. Since 2006, he has been faculty in the Mechanical Engineering Department, KAIST, Korea. His current research interests include fuel-saving technology, vehicle dynamics and control, and active safety systems. Prof. Choi is a Member of the American Society of Mechanical Engineers, the Society of Automotive Engineers, and the Korean Society of Automotive Engineers.